Paradigm Academic Press
Innovation in Science and Technology
ISSN 2788-7030
NOV. 2024 VOL.3, NO.6

Development of Landmark-Based Bit-State Model for Shape Analysis and Segmentation of Variations in Intima-Media Thickness of B-Mode Ultrasound Transverse Cross-Section of Carotid Artery Images

Charles Udekwe[1] & Ponnle Akinlolu[1]

[1] Federal University of Technology, Akure, Nigeria

Correspondence: Charles Udekwe, Federal University of Technology, Akure, Nigeria.

doi:10.56397/IST.2024.11.07

Abstract

Central to the assessment of carotid artery health is the measurement of intima-media thickness (IMT), a valuable diagnostic marker for atherosclerosis. IMT quantifies the thickness of two arterial layers — the intima and media — providing insights into arterial wall health and atherosclerotic changes. Carotid ultrasound, a non-invasive imaging technique, is the primary modality for IMT measurement. However, it is not without its challenges, including operator dependency and segmentation difficulties. To surmount these limitations and advance our understanding of carotid artery health, in this research paper, we develop the Bit-State model by applying landmark-based geometric morphometrics (GM) that built upon the foundation of cardinal point symmetry landmark distributed models (CPS-LDM) which we have developed in our previous papers to comprehensively characterize and segment carotid artery IMT, unveiling essential insights into variations and alterations. The Bit-State (BS) Model, revolutionizes our approach to understanding carotid artery structural variations. In this paper, there are four regions of interest (ROI) in the B-Mode carotid artery image, hence we designated each ROI as a bit. Each bit is capable of existing in either of two states: bit 1 as thick-walled and bit 0 as thin-walled ROI. In adopting this binary characterization, we generated 16 different modalities and variations of the ROI of the carotid artery, we then proceed to use the CPS-LD Model to formulate 16 equations for the segmentation of the ROI the carotid artery images. This new model simplifies the complexity of B-Mode ultrasound carotid artery images. It systematically characterizes shape variations using CPS-LDM equations, offering an interpretable framework for comprehending arterial wall composition. This research represents a significant leap forward in carotid artery health assessment, promising more precise diagnoses and targeted interventions for cardiovascular health. It highlights the pivotal role of landmark-based GM in addressing the challenges posed by carotid artery diseases and atherosclerosis. By pioneering this innovative model, this research paves the way for a deeper understanding of carotid artery health and its implications for stroke prevention — a critical stride towards mitigating the global burden of cardiovascular diseases.

Keywords: atherosclerosis, carotid arteries, intima-media thickness (IMT), Bit-State, landmarks

1. Introduction

Cardiovascular diseases (CVDs) are a group of disorders that affect the heart and blood vessels. They are the leading cause of death worldwide, accounting for over 30% of all deaths annually. CVDs can be caused by a variety of factors, including atherosclerosis, hypertension, diabetes, and smoking. (R. J. Esper & R. A. Nordaby, 2019). Atherosclerosis, a chronic and progressive vascular disorder, is characterized by the accumulation of atherosclerotic plaques within the walls of large and medium-sized arteries. These plaques primarily consist of lipids, inflammatory cells, smooth muscle cells, and connective tissue components (D. K. Arnett et al., 2019). Over time, atherosclerosis can affect various arteries, including the carotid arteries, which are responsible for supplying oxygenated blood to the brain. Atherosclerosis can lead to the development of atherosclerotic plaques within the carotid arteries. These plaques can narrow and stiffen the arterial walls. As the carotid arteries become affected by atherosclerosis, their ability to efficiently transport blood to the brain becomes compromised (A. Thapar, I. H. Jenkins, A. Mehta & A. H. Davies, 2013). Carotid stenosis is a condition characterized by the narrowing (stenosis) of the carotid arteries due to the buildup of atherosclerotic plaques. Severe carotid stenosis can significantly reduce blood flow to the brain. It can also increase the risk of embolization, where pieces of the plaque break off and travel to smaller brain arteries leading to ischemic stroke (Carotid Stenosis | Temple Health, n.d.).

The carotid arteries are paired blood vessels in the neck that supply oxygenated blood to the brain. They are named the common carotid arteries (CCA). Each CCA eventually bifurcates or splits into two smaller branches at a specific point within the neck. This bifurcation occurs at roughly the level of the upper border of the thyroid cartilage in the throat. The two branches that emerge from the bifurcation point are the internal carotid artery (ICA) and the external carotid artery (ECA). The ICA continues upward into the skull and supplies oxygenated blood to the brain. It is a critical vessel for cerebral circulation. The ECA supplies blood to the face, neck, and some of the external structures of the head. The bifurcation point of the common carotid artery is a common site for the development of atherosclerotic plaques (Carotid Stenosis | Temple Health, n.d.). Picture 1 shows the CCA, ICA and the ECA in a human accompanied by a healthy and diseased CCA.

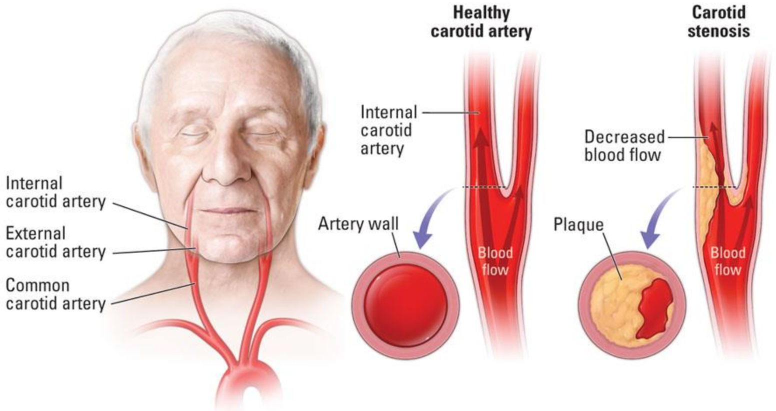

Picture 1. Images of Carotid Artery on Human Neck (Carotid Stenosis | Temple Health, n.d.)

Carotid artery disease, particularly at the bifurcation, is a significant risk factor for ischemic strokes (Ischemic Stroke (Clots): Causes, Symptoms & Treatment, n.d.). If a plaque within the carotid artery becomes unstable or ruptures, it can lead to the formation of a blood clot (thrombus) that can partially or completely block blood flow to the brain. These clots or emboli can result in a stroke if they travel to smaller cerebral arteries. Due to the importance of the strategic position of the bifurcation, the assessment and management of carotid artery disease at the CCA is of great clinical importance in stroke prevention (Management of symptomatic carotid atherosclerotic disease — UpToDate, n.d.).

The geometrical description of the transverse cross-section of the CCA typically resembles a circular or slightly oval shape with a smooth and symmetrical appearance. At the center of the cross-section is the arterial lumen, which appears as a hollow, open space. This lumen is where blood flows through. Surrounding the lumen is the innermost layer called the intima. It appears as a thin, smooth inner lining of the artery. Beyond the intima is the media, a thicker layer that consists of smooth muscle cells and elastic fibers. It appears as a uniform, relatively thick ring around the intima. The outermost layer is the adventitia, which appears as a fibrous layer surrounding the media. It provides structural support to the artery. In cases of atherosclerosis or carotid artery disease, plaques can develop within the artery wall. These plaques appear as irregular protrusions into the lumen, causing narrowing and irregularities in the otherwise smooth cross-sectional shape (E. Ukwatta et al., 2011).

Intima-media thickness (IMT) is a valuable marker used in the diagnosis and assessment of atherosclerosis in the carotid artery. It provides important information about the health of the arterial wall and the presence of atherosclerotic changes. Intima-media thickness refers to the measurement of the thickness of two layers of the arterial wall: the intima and the media. These measurements are typically taken using ultrasound imaging. In a healthy artery, the intima and media layers have minimal thickness, and there are no visible atherosclerotic plaques. However, in the presence of atherosclerosis, the intima layer becomes thicker due to the accumulation of fatty deposits, cholesterol, and inflammatory cells (atherosclerotic plaques)[1] (M. L. Bots, G. W. Evans, W. A. Riley & D. E. Grobbee, 2003).

IMT measurements are usually obtained through carotid ultrasound, a non-invasive imaging technique. During the ultrasound examination, high-frequency sound waves are used to create real-time images of the carotid arteries. These images show the layers of the arterial wall, including the intima and media. The technician or clinician measures the thickness of the intima and the combined thickness of the intima and media in specific segments of the carotid artery. An increase in intima-media thickness is considered an early sign of atherosclerosis, often before clinical symptoms become apparent. IMT measurements can help assess an individual's risk of cardiovascular events, such as heart attacks and strokes. Thicker intima-media layers are associated with a higher risk. Serial IMT measurements over time can track the progression or regression of atherosclerosis and the effectiveness of treatments (Carotid Intima-Media Thickness Test, n.d.; G. H. Kim & H. J. Youn, 2017). Picture 2 shows the geometric shape of the transverse cross-section of a CCA indicating the region of IMT measurement.

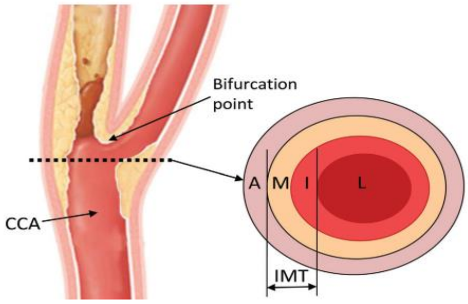

Picture 2. Carotid Arteries showing the Bifurcation point and the Transverse cross-section of a carotid artery showing the adventitia (A), media (M), intima (I), and lumen (L), as well as the IMT measurement (E. Ukwatta et al., 2011)

Ultrasound scans are the most widely used method for measuring IMT. Ultrasound is a non-invasive and relatively inexpensive imaging technique. However, ultrasound has two major demerits: (1) its accuracy depends on the skill and experience of the operator, and (2) it can be difficult to segment the carotid artery and measure IMT in the presence of artifacts (C. M. Moran & A. J. W. Thomson, 2020).

Several researchers have explored various methods for segmenting the carotid lumen-intima boundary (LIB) in transverse ultrasound (US) images. A. Zahalka and A. Fenster (2001) proposed a discrete dynamic contour model using gradient difference and gray level ratio for contour evolution, validated with seven transverse 2D slices. P. Abolmaesumi, M. R. Sirouspour & S. E. Salcudean (2000) used a star algorithm improved by Kalman filtering but lacked validation with human patient images. J. D. Gill, H. M. Ladak, D. A. Steinman, and A. Fenster (2000) introduced a semi-automatic method with a dynamic balloon model for 3D US, relying on seed points within the carotid artery. A. Zahalka and A. Fenster (2001) proposed a 3D US approach validated with phantom studies.

In the quest to combat these demerits and enhance our understanding of carotid artery health and the impact of atherosclerosis, landmark-based geometric morphometrics (GM) has risen as a powerful method. We had used this approach to develop the cardinal point symmetry landmark distribution model (CPS-LDM) to completely characterize and segment simulated thick-walled, phantom thin-walled and real in-vivo carotid artery images in our papers (C. N. Udekwe & A. A. Ponnle, 2019a; 2019b; 2021). In this paper, we leverage on anatomical landmarks and quantifiable measurements to analyze the shape and geometry of carotid artery IMT, offering valuable insights into variations and alterations of the ROI of B-Mode ultrasound carotid arteries. GM can be used to segment the carotid artery in a more accurate and reproducible manner than traditional methods (M. Webster & H. D. Sheets, 2010; H. Bogunović et al., 2012).

The remaining of this paper is organized as follows. Section II describes the proposed Bit-State model to capture the variations in the shapes of the ROIs of the B-Mode ultrasound carotid arteries in transverse cross-section. Section III discusses how the equations that characterizes the variations of the carotid artery shapes are derived using the CPS-LD Model. Conclusions are drawn in section IV.

[1] 9/20/23, 4:48 AM Intima-media thickness: appropriate evaluation and proper measurement https://www.escardio.org/Journals/E-Journal-of-Cardiology-Practice/Volume-13/Intima-media-thickness-Appropriate-evaluation-and-proper-measure… Intima-media thickness: appropriate evaluation and proper measurement, (2015). Available: https://www.escardio.org/Journals/E-Journal-of-Cardiology-Practice/Volume-13/Intima-media-thickness-Appropriate-evaluation-and-proper-measure

2. Bit-State Model to Capture Variations in Shapes of the ROIs

The introduction of the Bit-State (BS) Model in the context of B-Mode ultrasound carotid artery images represents an innovative approach to capturing and quantifying crucial information about the vascular structure. By designating each Region of Interest (ROI) as a bit, we transform the intricate details of the arterial wall into a binary representation, simplifying the complexity of the data. In this unique framework, the region of interest (ROI) of a B-Mode ultrasound image of the carotid artery is distilled into a series of four bits, each capable of adopting one of two states: bit 1 for thick-walled regions and bit 0 for thin-walled regions. This approach holds promise for several reasons. Firstly, it enables the concise representation of the carotid artery's structural variations, allowing for a streamlined analysis of key features. Secondly, the use of binary states facilitates the development of a systematic Bit-State Model, offering a clear and interpretable framework for understanding the arterial wall's composition and characteristics.

The introduction of the BS Model propels us into an exciting realm of research, where we aim to formulate a comprehensive set of equations that captures the entirety of shape variations within the carotid artery's Region of Interest (ROI). Building upon the foundation of cardinal point symmetry landmark distributed models (CPS-LDM) developed in previous papers (C. N. Udekwe & A. A. Ponnle, 2019a; 2019b; 2021), this innovative approach seeks to create a unified framework capable of describing all conceivable shape variations.

In doing so, we equip ourselves with a powerful tool to systematically characterize structural changes within the ROI of the carotid artery. This framework promises to enhance our capacity to detect, understand, and differentiate variations in shape, which is of paramount importance in the field of cardiovascular health.

Table 1 outlines the various potential shape variations observed in the ROIs of B-Mode transverse cross-sections of ultrasound carotid artery images through the Bit-State model.

Table 1. Bit-State Look-up Truth Table Outlining the Variations in Shapes of ROIs in B-Mode Ultrasound Carotid Artery

S/N	**Model Tag**	**ROIs**				**Bit-State**
		1	**2**	**3**	**4**	
1	BS(1)-LDM	0	0	0	0	0000 (All Thin)
2	BS(2)-LDM	0	0	0	1	0001
3	BS(3)-LDM	0	0	1	0	0010
4	BS(4)-LDM	0	0	1	1	0011
5	BS(5)-LDM	0	1	0	0	0100
6	BS(6)-LDM	0	1	0	1	0101
7	BS(7)-LDM	0	1	1	0	0110
8	BS(8)-LDM	0	1	1	1	0111
9	BS(9)-LDM	1	0	0	0	1000
10	BS(10)-LDM	1	0	0	1	1001
11	BS(11)-LDM	1	0	1	0	1010
12	BS(12)-LDM	1	0	1	1	1011
13	BS(13)-LDM	1	1	0	0	1100
14	BS(14)-LDM	1	1	0	1	1101
15	BS(15)-LDM	1	1	1	0	1110
16	BS(16)-LDM	1	1	1	1	1111 (All thick)

3. CPS-LDM Equations for Each Bit-State as Shown in Table 1

In this section, we discuss the derivation of the equations for each possible shape variation of the ROIs of a transverse section B-Mode ultrasound carotid artery as depicted in the look-up table.

3.1 BS(1)-LDM (0 0 0 0) (All ROI are THIN)

The boundary shape for this tag is shown in Figure 1:

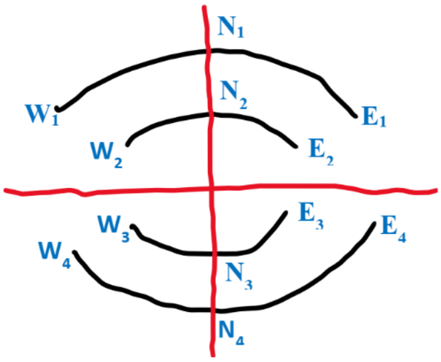

Figure 1. BS(1)-LDM (0 0 0 0) Tag

As shown in Figure 1, this tag indicates that the four ROIs are thin-walled. The CPS-LDM equation for the total landmarks (TL_{Tag1}) required to completely characterize this thin-walled carotid artery images for complete segmentation has been derived in this paper (C. N. Udekwe & A. A. Ponnle, 2019b). The equation (1) shows the final equation that was obtained:

$$TL_{Tag1} = \underbrace{3U_M}_{FLs} + \underbrace{\begin{bmatrix} K_{NWE}^{1,4} \\ K_{NWE}^{2,3} \end{bmatrix}}_{MLs} \quad (1)$$

Where;

FLs is the number of fixed landmarks in any given ROI.

U is the number of ROI bit to be described.

The subscript M is the position of the bit of the ROI to be described, (Here, M = 1,2,3,4).

MLs is the number dynamic landmarks on any given ROI.

(K_{CP}^{ROI}) notation represents the number of integer landmarks that can be annotated on a given ROI boundary.

The superscript ROI is the is the bit position of the ROI under consideration.

The subscript CP is the type of cardinal point used to describe the ROI bit (CP = NW, NE, etc.).

3.2 BS(2)-LDM (0 0 0 1); (ROI 1 - 3 Are THIN; ROI 4 Is THICK)

The boundary shape for this tag is shown in Figure 2:

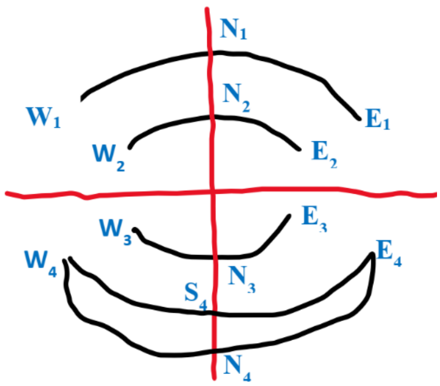

Figure 2. BS(2)-LDM (0 0 0 1) Tag

Using the CPS-LD model, the total landmark for Figure 2 is given as;

$$TL_{Tag2} = FL_{Tag2} + ML_{Tag2} \quad (2)$$

Figure 2 is different from the geometrical boundary shape equations derived in [paper 1] and [paper 2] because it is a mixture of thick and thin ROIs, hence there will be some modifications to the equations earlier derived in [paper 1] and [paper 2].

Here is how we obtain the equation for the FLs.

$$FL_{Tag2} = 3U_{Mthn} + 4U_{Mthk} \tag{3}$$

Where;

Subscript M_{thn} describe the bit position of the ROIs, (here, M_{thn}= 1,2, and 3)

Subscript M_{thk} describes the bit position of the ROIs, (here, M_{thk} = 4)

In Figure 2, $U_{Mthn} = 3$, and $U_{Mthk} = 1$, hence, the number of FL_{Tag2} is obtained as;

$$FL_{Tag2} = 3U_{1-3} + 4U_4 \tag{4}$$

$$FL_{Tag2} = 3 \times 3 + 4 \times 1$$

$$FL_{Tag2} = 13$$

This implies that 13 FL_{Tag2} are needed to characterize the geometrical boundary shape of the ROIs in Figure 2. Following the notations described in [paper 1] and [paper 2], we derive the movable landmarks (ML_{Tag2}) of Figure 2 as follows;

$$ML_{Tag2} = (NW)_1 + (NE)_1 + (NW)_2 + (NE)_2 + (NW)_3 + (NE)_3$$
$$+(NW)_4 + (NE)_4 + (SW)_4 + (SE)_4 \tag{5}$$

Applying symmetry conditions, we simplify equation (5) to become equation (6);

$$ML_{Tag2} = K_{WNE}^1 + K_{WNE}^2 + K_{WNE}^3 + K_{WNE}^4 + K_{WSE}^4 \tag{6}$$

Applying mirror-image conditions, equation (6) becomes;

$$ML_{Tag2} = K_{WNE}^{1,4} + K_{WNE}^{2,3} + K_{WSE}^4 \tag{7}$$

Rearranging equation (7) in a matrix-like form becomes

$$ML_{Tag2} = \begin{bmatrix} K_{WNE}^{1,4} & K_{WSE}^4 \\ K_{WNE}^{2,3} & - \end{bmatrix} \tag{8}$$

From equations (2), (4), and (8), the TLs equation becomes;

$$TL_{Tag2} = 3U_{1-3} + 4U_4 + \begin{bmatrix} K_{WNE}^{1,4} & K_{WSE}^4 \\ K_{WNE}^{2,3} & - \end{bmatrix} \tag{9}$$

We will use the same technique utilized in deriving the equations for tag 2 to obtain equations for tag 3 to tag 15.

3.3 BS(3)-LDM (0 0 1 0); (ROI 1, 2, and 4 Are THIN; ROI 3 Is THICK)

The boundary shape for this tag is shown in Figure 3;

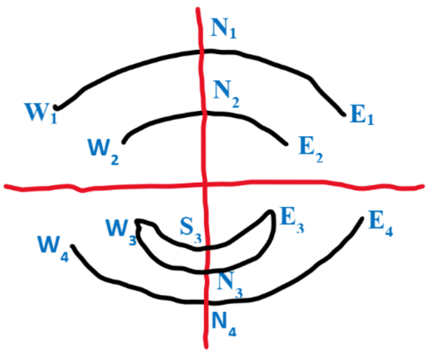

Figure 3. BS(3)-LDM (0 0 1 0) Tag

Using the CPS-LD model, we derive the equation for TL_{Tag3} for Tag 3.

$$TL_{Tag3} = FL_{Tag3} + ML_{Tag3}$$

The FL_{Tag3} equation is derived as follows

$$FL_{Tag3} = 3U_{Mthn} + 4U_{Mthk};$$

Where;

$$U_{Mthn} = 3,\ U_{Mthk} = 1, M_{thn} = 1,2, 4, \text{ and } M_{thk} = 3.$$

Hence,

$$FL_{Tag3} = 3U_{1-2,4} + 4U_3 \tag{10}$$

The ML_{Tag3} equation is derived as follows

$$ML_{Tag3} = (NW)_1 + (NE)_1 + (NW)_2 + (NE)_2 + (NW)_3 + (NE)_3 \\ +(SW)_3 + (SE)_3 + (NW)_4 + (NE)_4 \tag{11}$$

Applying symmetry conditions, equation (11) becomes;

$$ML_{Tag3} = K_{WNE}^1 + K_{WNE}^2 + K_{WNE}^3 + K_{WSE}^3 + K_{WNE}^4 \tag{12}$$

Applying mirror-image conditions, equation (12) becomes;

$$ML_{Tag3} = K_{WNE}^{1,4} + K_{WNE}^{2,3} + K_{WSE}^3 \tag{13}$$

Rearranging equation (13) in a matrix-like form becomes

$$ML_{Tag3} = \begin{bmatrix} K_{WNE}^{1,4} & - \\ K_{WNE}^{2,3} & K_{WSE}^3 \end{bmatrix} \tag{14}$$

From equations (10), and (14), the TL_{Tag3} equation becomes;

$$TL_{Tag3} = 3U_{1-2,4} + 4U_3 + \begin{bmatrix} K_{WNE}^{1,4} & - \\ K_{WNE}^{2,3} & K_{WSE}^3 \end{bmatrix} \tag{15}$$

3.4 BS(4)-LDM (0 0 1 1); (ROI 1 and 2 Are THIN; ROI 3 and 4 Are THICK)

The boundary shape for this tag is shown in Figure 4;

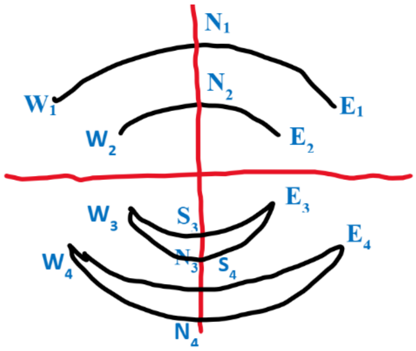

Figure 4. BS(4)-LDM (0 0 1 1) Tag

Using the CPS-LD model, we derive the equation for TL_{Tag4} for Tag 4.

$$TL_{Tag4} = FL_{Tag4} + ML_{Tag4}$$

The FL_{Tag4} equation is derived as follows:

$$FL_{Tag4} = 3U_{Mthn} + 4U_{Mthk};$$

Where;

$$U_{Mthn} = 2, U_{Mthk} = 2, M_{thn} = 1 \text{ and } 2, \text{ and } M_{thk} = 3 \text{ and } 4.$$

Hence,

$$FL_{Tag4} = 3U_{1-2} + 4U_{3-4} \tag{16}$$

The ML_{Tag4} equation is derived as follows:

$$ML_{Tag4} = (NW)_1 + (NE)_1 + (NW)_2 + (NE)_2 + (NW)_3 + (NE)_3 \\ +(SW)_3 + (SE)_3 + (NW)_4 + (NE)_4 + (SW)_4 + (SE)_4 \tag{17}$$

Applying symmetry conditions, equation (17) becomes;

$$ML_{Tag4} = K_{WNE}^1 + K_{WNE}^2 + K_{WNE}^3 + K_{WSE}^3 + K_{WNE}^4 + K_{WSE}^4 \tag{18}$$

Applying mirror-image conditions, equation (18) becomes;

$$ML_{Tag4} = K_{WNE}^{1,4} + K_{WNE}^{2,3} + K_{WSE}^{3} + K_{WSE}^{4} \tag{19}$$

Rearranging equation (19) in a matrix-like form becomes

$$ML_{Tag4} = \begin{bmatrix} K_{WNE}^{1,4} & K_{WSE}^{4} \\ K_{WNE}^{2,3} & K_{WSE}^{3} \end{bmatrix} \tag{20}$$

From equations (16), and (20), the TL_{Tag4} equation becomes;

$$TL_{Tag4} = 3U_{1-2} + 4U_{3-4} + \begin{bmatrix} K_{WNE}^{1,4} & K_{WSE}^{4} \\ K_{WNE}^{2,3} & K_{WSE}^{3} \end{bmatrix} \tag{21}$$

3.5 BS(5)-LDM (0 1 0 0); (ROI 1, 3 and 4 Are THIN; ROI 2 Is THICK)

The boundary shape for this tag is shown in Figure 5:

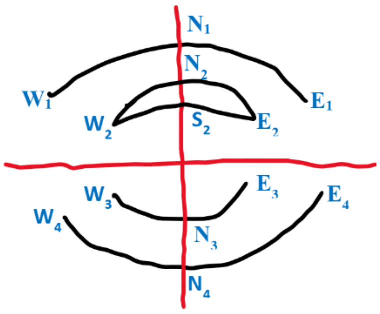

Figure 5. BS(5)-LDM (0 1 0 0) Tag

Using the CPS-LD model, we derive the equation for TL_{Tag5} for Tag 5.

$$TL_{Tag5} = FL_{Tag5} + ML_{Tag5}$$

The FL_{Tag5} equation is derived as follows:

$$FL_{Tag5} = 3U_{Mthn} + 4U_{Mthk};$$

Where;

$$U_{Mthn} = 3,\ U_{Mthk} = 1,\ M_{thn} = 1,\ 3\text{-}4, \text{ and } M_{thk} = 2.$$

Hence,

$$FL_{Tag5} = 3U_{1,3-4} + 4U_2 \tag{22}$$

The ML_{Tag5} equation is derived as follows;

$$ML_{Tag5} = (NW)_1 + (NE)_1 + (NW)_2 + (NE)_2 + (SW)_2 + (SE)_2 + (NW)_3 + (NE)_3 + (NW)_4 + (NE)_4 \tag{23}$$

Applying symmetry conditions, equation (23) becomes;

$$ML_{Tag5} = K_{WNE}^{1} + K_{WNE}^{2} + K_{WSE}^{2} + K_{WNE}^{3} + K_{WNE}^{4} \tag{24}$$

Applying mirror-image conditions, equation (24) becomes;

$$ML_{Tag5} = K_{WNE}^{1,4} + K_{WNE}^{2,3} + K_{WSE}^{2} \tag{25}$$

Rearranging equation (25) in a matrix-like form becomes

$$ML_{Tag5} = \begin{bmatrix} K_{WNE}^{1,4} & - \\ K_{WNE}^{2,3} & K_{WSE}^{2} \end{bmatrix} \tag{26}$$

From equations (22), and (26), the TL_{Tag5} equation becomes;

$$TL_{Tag5} = 3U_{1,3-4} + 4U_2 + \begin{bmatrix} K_{WNE}^{1,4} & - \\ K_{WNE}^{2,3} & K_{WSE}^{2} \end{bmatrix} \tag{27}$$

3.6 BS(6)-LDM (0 1 0 1); (ROI 1 and 3 Are THIN; ROI 2 and 4 Are THICK)

The boundary shape for this tag is shown in Figure 6:

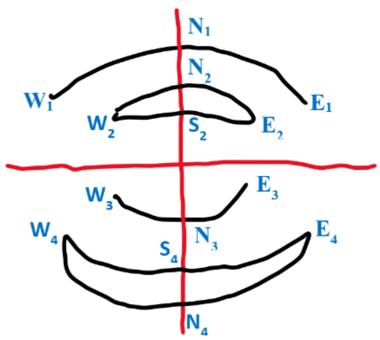

Figure 6. BS(6)-LDM (0 1 0 1) Tag

Using the CPS-LD model, we derive the equation for TL_{Tag6} for Tag 6.

$$TL_{Tag6} = FL_{Tag6} + ML_{Tag6}$$

The FL_{Tag6} equation is derived as follows:

$$FL_{Tag6} = 3U_{Mthn} + 4U_{Mthk};$$

Where;

$U_{Mthn} = 2$, $U_{Mthk} = 2$, $M_{thn} = 2$ and 4, and $M_{thk} = 2$.

Hence,

$$FL_{Tag6} = 3U_{1,3} + 4U_{2,4} \tag{28}$$

The ML_{Tag6} equation is derived as follows:

$$ML_{Tag6} = (NW)_1 + (NE)_1 + (NW)_2 + (NE)_2 + (SW)_2 + (SE)_2 + (NW)_3 + (NE)_3 + (NW)_4 + (NE)_4 + (SW)_4 + (SE)_4 \tag{29}$$

Applying symmetry conditions, equation (29) becomes;

$$ML_{Tag6} = K^1_{WNE} + K^2_{WNE} + K^2_{WSE} + K^3_{WNE} + K^4_{WNE} + K^4_{WSE} \tag{30}$$

Applying mirror-image conditions, equation (30) becomes;

$$ML_{Tag6} = K^{1,4}_{WNE} + K^{2,3}_{WNE} + K^2_{WSE} + K^4_{WSE} \tag{31}$$

Rearranging equation (31) in a matrix-like form becomes;

$$ML_{Tag6} = \begin{bmatrix} K^{1,4}_{WNE} & K^4_{WSE} \\ K^{2,3}_{WNE} & K^2_{WSE} \end{bmatrix} \tag{32}$$

From equations (28), and (32), the TL_{Tag6} equation becomes;

$$TL_{Tag6} = 3U_{1,3} + 4U_{2,4} + \begin{bmatrix} K^{1,4}_{WNE} & K^4_{WSE} \\ K^{2,3}_{WNE} & K^2_{WSE} \end{bmatrix} \tag{33}$$

3.7 BS(7)-LDM (0 1 1 0); (ROI 1 and 4 Are THIN; ROI 2 and 3 Are THICK)

The boundary shape for this tag is shown in Figure 7:

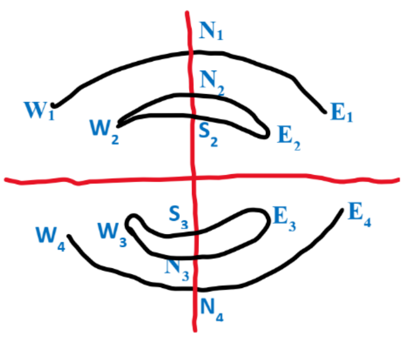

Figure 7. BS(7)-LDM (0 1 0 1) Tag

Using the CPS-LD model, we derive the equation for TL_{Tag7} for Tag 7.

$$TL_{Tag7} = FL_{Tag7} + ML_{Tag7}$$

The FL_{Tag7} equation is derived as follows:

$$FL_{Tag7} = 3U_{Mthn} + 4U_{Mthk};$$

Where;

$$U_{Mthn} = 2,\ U_{Mthk} = 2,\ M_{thn} = 1 \text{ and } 4, \text{ and } M_{thk} = 2 \text{ and } 3.$$

Hence,

$$FL_{Tag7} = 3U_{1,4} + 4U_{2-3} \tag{34}$$

The ML_{Tag7} equation is derived as follows:

$$ML_{Tag7} = (NW)_1 + (NE)_1 + (NW)_2 + (NE)_2 + (SW)_2 + (SE)_2 + (NW)_3 \\ +(NE)_3 + (SW)_3 + (SE)_3 + (NW)_4 + (NE)_4 \tag{35}$$

Applying symmetry conditions, equation (35) becomes;

$$ML_{Tag7} = K^1_{WNE} + K^2_{WNE} + K^2_{WSE} + K^3_{WNE} + K^3_{WSE} + K^4_{WNE} \tag{36}$$

Applying mirror-image conditions, equation (36) becomes;

$$ML_{Tag7} = K^{1,4}_{WNE} + K^{2,3}_{WNE} + K^{2,3}_{WSE} \tag{37}$$

Rearranging equation (37) in a matrix-like form becomes;

$$ML_{Tag7} = \begin{bmatrix} K^{1,4}_{WNE} & - \\ K^{2,3}_{WNE} & K^{2,3}_{WSE} \end{bmatrix} \tag{38}$$

From equations (34), and (38), the TL_{Tag7} equation becomes;

$$TL_{Tag7} = 3U_{1,4} + 4U_{2-3} + \begin{bmatrix} K^{1,4}_{WNE} & - \\ K^{2,3}_{WNE} & K^{2,3}_{WSE} \end{bmatrix} \tag{39}$$

3.8 BS(8)-LDM (0 1 1 1); (ROI 1 Is THIN; ROI 2-4 Are THICK)

The boundary shape for this tag is shown in Figure 8:

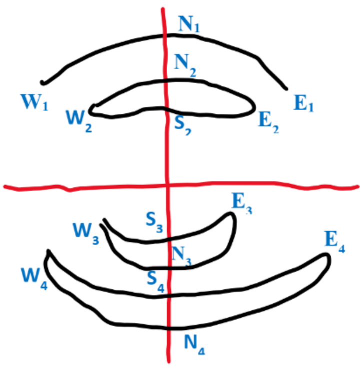

Figure 8. BS(8)-LDM (0 1 1 1) Tag

Using the CPS-LD model, we derive the equation for TL_{Tag8} for Tag 8.

$$TL_{Tag8} = FL_{Tag8} + ML_{Tag8}$$

The FL_{Tag8} equation is derived as follows:

$$FL_{Tag8} = 3U_{Mthn} + 4U_{Mthk};$$

Where;

$$U_{Mthn} = 1,\ U_{Mthk} = 3,\ M_{thn} = 1, \text{ and } M_{thk} = 2 - 4.$$

Hence,

$$FL_{Tag8} = 3U_1 + 4U_{2-4} \tag{40}$$

The ML_{Tag8} equation is derived as follows:

$$ML_{Tag8} = (NW)_1 + (NE)_1 + (NW)_2 + (NE)_2 + (SW)_2 + (SE)_2 + (NW)_3 + (NE)_3 + (SW)_3 + (SE)_3 + (NW)_4 + (NE)_4 + (SW)_4 + (SE)_4 \quad (41)$$

Applying symmetry conditions, equation (41) becomes;

$$ML_{Tag8} = K_{WNE}^{1} + K_{WNE}^{2} + K_{WSE}^{2} + K_{WNE}^{3} + K_{WSE}^{3} + K_{WNE}^{4} + K_{WSE}^{4} \quad (42)$$

Applying mirror-image conditions, equation (42) becomes;

$$ML_{Tag8} = K_{WNE}^{1,4} + K_{WNE}^{2,3} + K_{WSE}^{2,3} + K_{WSE}^{4} \quad (43)$$

Rearranging equation (43) in a matrix-like form becomes;

$$ML_{Tag8} = \begin{bmatrix} K_{WNE}^{1,4} & K_{WSE}^{4} \\ K_{WNE}^{2,3} & K_{WSE}^{2,3} \end{bmatrix} \quad (44)$$

From equations (40), and (44), the TL_{Tag8} equation becomes;

$$TL_{Tag8} = 3U_1 + 4U_{2-4} + \begin{bmatrix} K_{WNE}^{1,4} & K_{WSE}^{4} \\ K_{WNE}^{2,3} & K_{WSE}^{2,3} \end{bmatrix} \quad (45)$$

3.9 BS(9)-LDM (1 0 0 0); (ROI 2 - 4 Are THIN; ROI 1 Is THICK)

The boundary shape for this tag is shown in Figure 9:

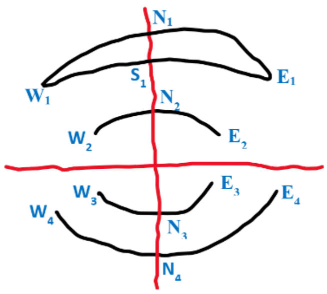

Figure 9. BS(9)-LDM (1 0 0 0) Tag

Using the CPS-LD model, we derive the equation for TL_{Tag9} for Tag 9.

$$TL_{Tag9} = FL_{Tag9} + ML_{Tag9}$$

The FL_{Tag9} equation is derived as follows:

$$FL_{Tag9} = 3U_{Mthn} + 4U_{Mthk};$$

Where;

$U_{Mthn} = 3$, $U_{Mthk} = 1$, $M_{thn} = 2 - 4$, and $M_{thk} = 1$.

Hence,

$$FL_{Tag9} = 3U_{2-4} + 4U_1 \quad (46)$$

The ML_{Tag9} equation is derived as follows:

$$ML_{Tag9} = (NW)_1 + (NE)_1 + (SW)_1 + (SE)_1 + (NW)_2 + (NE)_2 + (NW)_3 + (NE)_3 + (NW)_4 + (NE)_4 \quad (47)$$

Applying symmetry conditions, equation (47) becomes;

$$ML_{Tag9} = K_{WNE}^{1} + K_{WSE}^{1} + K_{WNE}^{2} + K_{WNE}^{3} + K_{WNE}^{4} \quad (48)$$

Applying mirror-image conditions, equation (48) becomes;

$$ML_{Tag9} = K_{WNE}^{1,4} + K_{WNE}^{2,3} + K_{WSE}^{1} \quad (49)$$

Rearranging equation (49) in a matrix-like form becomes;

$$ML_{Tag9} = \begin{bmatrix} K_{WNE}^{1,4} & K_{WSE}^{1} \\ K_{WNE}^{2,3} & - \end{bmatrix} \quad (50)$$

From equations (46), and (50), the TL_{Tag9} equation becomes;

$$TL_{Tag9} = 3U_{2-4} + 4U_1 + \begin{bmatrix} K_{WNE}^{1,4} & K_{WSE}^{1} \\ K_{WNE}^{2,3} & - \end{bmatrix} \quad (51)$$

3.10 BS(10)-LDM (1 0 0 1); (ROI 1 and 4 Are THIN; ROI 2 -3 Are THICK)

The boundary shape for this tag is shown in Figure 10:

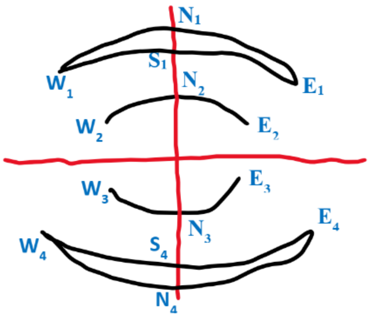

Figure 10. BS(10)-LDM (1 0 0 1) Tag

Using the CPS-LD model, we derive the equation for TL_{Tag10} for Tag 10.

$$TL_{Tag10} = FL_{Tag10} + ML_{Tag10}$$

The FL_{Tag10} equation is derived as follows:

$$FL_{Tag10} = 3U_{Mthn} + 4U_{Mthk};$$

Where;

$$U_{Mthn} = 2,\ U_{Mthk} = 2, M_{thn} = 2 - 3, \text{ and } M_{thk} = 1 - 4.$$

Hence,

$$FL_{Tag10} = 3U_{2-3} + 4U_{1,4} \quad (52)$$

The ML_{Tag10} equation is derived as follows:

$$ML_{Tag10} = (NW)_1 + (NE)_1 + (SW)_1 + (SE)_1 + (NW)_2 + (NE)_2 + (NW)_3 + (NE)_3 + (NW)_4 + (NE)_4 + (SW)_4 + (SE)_4 \quad (53)$$

Applying symmetry conditions, equation (53) becomes;

$$ML_{Tag10} = K_{WNE}^{1} + K_{WSE}^{1} + K_{WNE}^{2} + K_{WNE}^{3} + K_{WNE}^{4} + K_{WSE}^{4} \quad (54)$$

Applying mirror-image conditions, equation (54) becomes;

$$ML_{Tag10} = K_{WNE}^{1,4} + K_{WNE}^{2,3} + K_{WSE}^{1,4} \quad (55)$$

Rearranging equation (55) in a matrix-like form becomes;

$$ML_{Tag10} = \begin{bmatrix} K_{WNE}^{1,4} & K_{WSE}^{1,4} \\ K_{WNE}^{2,3} & - \end{bmatrix} \quad (56)$$

From equations (52), and (56), the TL_{Tag10} equation becomes;

$$TL_{Tag10} = 3U_{2-3} + 4U_{1,4} + \begin{bmatrix} K_{WNE}^{1,4} & K_{WSE}^{1,4} \\ K_{WNE}^{2,3} & - \end{bmatrix} \quad (56)$$

3.11 BS(11)-LDM (1 0 1 0); (ROI 2 and 4 Are THIN; ROI 1 and 3 Are THICK)

The boundary shape for this tag is shown in Figure 11:

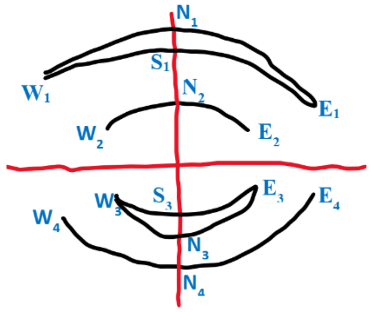

Figure 11. BS(11)-LDM (1 0 1 0) Tag

Using the CPS-LD model, we derive the equation for TL_{Tag11} for Tag 11.

$$TL_{Tag11} = FL_{Tag11} + ML_{Tag11}$$

The FL_{Tag11} equation is derived as follows:

$$FL_{Tag11} = 3U_{Mthn} + 4U_{Mthk};$$

Where;

$U_{Mthn} = 2$, $U_{Mthk} = 2$, M_{thn} = 2 and 4, and M_{thk} = 1 and 3.

Hence,

$$FL_{Tag11} = 3U_{2,4} + 4U_{1,3} \tag{57}$$

The ML_{Tag11} equation is derived as follows:

$$ML_{Tag11} = (NW)_1 + (NE)_1 + (SW)_1 + (SE)_1 + (NW)_2 + (NE)_2 + (NW)_3$$
$$+(NE)_3 + (SW)_3 + (SE)_3 + (NW)_4 + (NE)_4 \tag{58}$$

Applying symmetry conditions, equation (58) becomes;

$$ML_{Tag11} = K^1_{WNE} + K^1_{WSE} + K^2_{WNE} + K^3_{WNE} + K^3_{WSE} + K^4_{WNE} \tag{59}$$

Applying mirror-image conditions, equation (59) becomes;

$$ML_{Tag11} = K^{1,4}_{WNE} + K^{2,3}_{WNE} + K^1_{WSE} + K^3_{WSE} \tag{60}$$

Rearranging equation (60) in a matrix-like form becomes;

$$ML_{Tag11} = \begin{bmatrix} K^{1,4}_{WNE} & K^1_{WSE} \\ K^{2,3}_{WNE} & K^3_{WSE} \end{bmatrix} \tag{61}$$

From equations (57), and (61), the TL_{Tag11} equation becomes;

$$TL_{Tag11} = 3U_{2,4} + 4U_{1,3} + \begin{bmatrix} K^{1,4}_{WNE} & K^1_{WSE} \\ K^{2,3}_{WNE} & K^3_{WSE} \end{bmatrix} \tag{62}$$

3.12 BS(12)-LDM (1 0 1 1); (ROI 2 Is THIN; ROI 1, 3 - 4 Are THICK)

The boundary shape for this tag is shown in Figure 12:

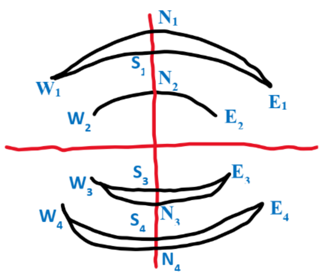

Figure 12. BS(12)-LDM (1 0 1 1) Tag

Using the CPS-LD model, we derive the equation for TL_{Tag12} for Tag 12.

$$TL_{Tag12} = FL_{Tag12} + ML_{Tag12}$$

The FL_{Tag12} equation is derived as follows:

$$FL_{Tag12} = 3U_{Mthn} + 4U_{Mthk};$$

Where;

$U_{Mthn} = 1$, $U_{Mthk} = 3$, $M_{thn} = 2$, and $M_{thk} = 1, 3 - 4$.

Hence,

$$FL_{Tag12} = 3U_3 + 4U_{1,3-4} \tag{63}$$

The ML_{Tag12} equation is derived as follows:

$$ML_{Tag12} = (NW)_1 + (NE)_1 + (SW)_1 + (SE)_1 + (NW)_2 + (NE)_2 + (NW)_3$$
$$+(NE)_3 + (SW)_3 + (SE)_3 + (NW)_4 + (NE)_4 + (SW)_4 + (SE)_4 \tag{64}$$

Applying symmetry conditions, equation (64) becomes;

$$ML_{Tag12} = K^1_{WNE} + K^1_{WSE} + K^2_{WNE} + K^3_{WNE} + K^3_{WSE} + K^4_{WNE} + K^4_{WSE} \tag{65}$$

Applying mirror-image conditions, equation (65) becomes;

$$ML_{Tag12} = K^{1,4}_{WNE} + K^{2,3}_{WNE} + K^{1,4}_{WSE} + K^3_{WSE} \tag{66}$$

Rearranging equation (66) in a matrix-like form becomes;

$$ML_{Tag12} = \begin{bmatrix} K^{1,4}_{WNE} & K^{1,4}_{WSE} \\ K^{2,3}_{WNE} & K^3_{WSE} \end{bmatrix} \tag{67}$$

From equations (63), and (67), the TL_{Tag12} equation becomes;

$$TL_{Tag12} = 3U_3 + 4U_{1,3-4} + \begin{bmatrix} K^{1,4}_{WNE} & K^{1,4}_{WSE} \\ K^{2,3}_{WNE} & K^3_{WSE} \end{bmatrix} \tag{68}$$

3.13 BS(13)-LDM (1 1 0 0); (ROI 1 - 2 Are THIN; ROI 3 - 4 Are THICK)

The boundary shape for this tag is shown in Figure 13:

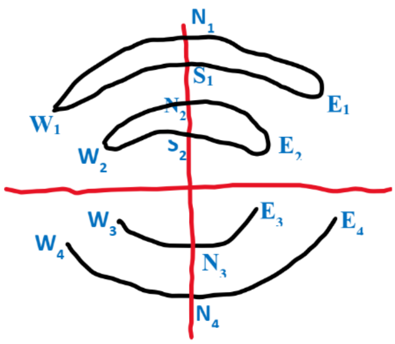

Figure 13. BS(13)-LDM (1 1 0 0) Tag

Using the CPS-LD model, we derive the equation for TL_{Tag13} for Tag 13.

$$TL_{Tag13} = FL_{Tag13} + ML_{Tag13}$$

The FL_{Tag13} equation is derived as follows:

$$FL_{Tag13} = 3U_{Mthn} + 4U_{Mthk};$$

Where;

$U_{Mthn} = 2$, $U_{Mthk} = 2$, $M_{thn} = 1 - 2$, and $M_{thk} = 3 - 4$.

Hence,

$$FL_{Tag13} = 3U_{1-2} + 4U_{3-4} \tag{69}$$

The ML_{Tag13} equation is derived as follows:

$$ML_{Tag13} = (NW)_1 + (NE)_1 + (SW)_1 + (SE)_1 + (NW)_2 + (NE)_2 + (SW)_2 + (SE)_2$$

$$+(NE)_3 \ +(NW)_3 + (NE)_4 + (NW)_4 \quad (70)$$

Applying symmetry conditions, equation (70) becomes;

$$ML_{Tag13} = K^1_{WNE} + K^1_{WSE} + K^2_{WNE} + K^2_{WSE} + K^3_{WNE} + K^4_{WNE} \quad (71)$$

Applying mirror-image conditions, equation (71) becomes;

$$ML_{Tag13} = K^{1,4}_{WNE} + K^{2,3}_{WNE} + K^1_{WSE} + K^2_{WSE} \quad (72)$$

Rearranging equation (72) in a matrix-like form becomes;

$$ML_{Tag13} = \begin{bmatrix} K^{1,4}_{WNE} & K^1_{WSE} \\ K^{2,3}_{WNE} & K^2_{WSE} \end{bmatrix} \quad (73)$$

From equations (69), and (73), the TL_{Tag13} equation becomes;

$$TL_{Tag13} = 3U_{1-2} + 4U_{3-4} + \begin{bmatrix} K^{1,4}_{WNE} & K^1_{WSE} \\ K^{2,3}_{WNE} & K^2_{WSE} \end{bmatrix} \quad (74)$$

3.14 BS(14)-LDM (1 1 0 1); (ROI 3 Is THIN; ROI 1 – 2, 4 Are THICK)

The boundary shape for this tag is shown in Figure 14:

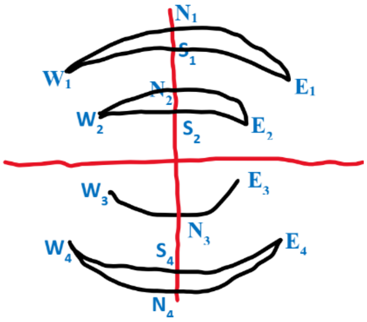

Figure 14. BS(14)-LDM (1 1 0 1) Tag

Using the CPS-LD model, we derive the equation for TL_{Tag14} for Tag 14.

$$TL_{Tag14} = FL_{Tag14} + ML_{Tag14}$$

The FL_{Tag14} equation is derived as follows:

$$FL_{Tag14} = 3U_{Mthn} + 4U_{Mthk};$$

Where;

$$U_{Mthn} = 1, U_{Mthk} = 3, M_{thn} = 3, \text{ and } M_{thk} = 1 - 2, 4$$

Hence,

$$FL_{Tag14} = 3U_3 + 4U_{1-2,4} \quad (75)$$

The ML_{Tag14} equation is derived as follows

$$ML_{Tag14} = (NW)_1 + (NE)_1 + (SW)_1 + (SE)_1 + (NW)_2 + (NE)_2 + (SW)_2 + (SE)_2$$
$$+(NE)_3 + (NW)_3 + (NE)_4 + (NW)_4 + (SW)_4 + (SE)_4 \quad (76)$$

Applying symmetry conditions, equation (76) becomes;

$$ML_{Tag14} = K^1_{WNE} + K^1_{WSE} + K^2_{WNE} + K^2_{WSE} + K^3_{WNE} + K^4_{WNE} + K^4_{WSE} \quad (77)$$

Applying mirror-image conditions, equation (77) becomes;

$$ML_{Tag14} = K^{1,4}_{WNE} + K^{1,4}_{WSE} + K^{2,3}_{WNE} + K^2_{WSE} \quad (78)$$

Rearranging equation (78) in a matrix-like form becomes;

$$ML_{Tag14} = \begin{bmatrix} K^{1,4}_{WNE} & K^{1,4}_{WSE} \\ K^{2,3}_{WNE} & K^2_{WSE} \end{bmatrix} \quad (78)$$

From equations (75), and (78), the TL_{Tag14} equation becomes;

$$TL_{Tag14} = 3U_3 + 4U_{1-2,4} + \begin{bmatrix} K_{WNE}^{1,4} & K_{WSE}^{1,4} \\ K_{WNE}^{2,3} & K_{WSE}^{2} \end{bmatrix} \quad (79)$$

3.15 BS(15)-LDM (1 1 1 0); (ROI 4 Is THIN; ROI 1 – 3 Are THICK)

The boundary shape for this tag is shown in Figure 15:

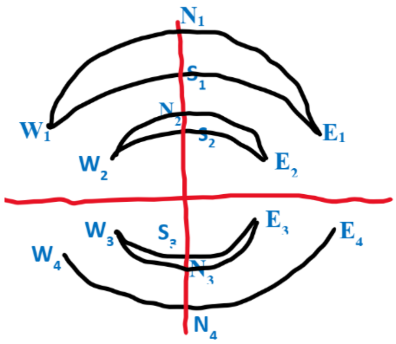

Figure 15. BS(15)-LDM (1 1 1 0) Tag

Using the CPS-LD model, we derive the equation for TL_{Tag15} for Tag 15.

$$TL_{Tag15} = FL_{Tag15} + ML_{Tag15}$$

The FL_{Tag15} equation is derived as follows:

$$FL_{Tag15} = 3U_{Mthn} + 4U_{Mthk};$$

Where;

$$U_{Mthn} = 1,\ U_{Mthk} = 3,\ M_{thn} = 1 - 3, \text{ and } M_{thk} = 4$$

Hence,

$$FL_{Tag15} = 3U_4 + 4U_{1-3} \quad (80)$$

The ML_{Tag15} equation is derived as follows:

$$ML_{Tag15} = (NW)_1 + (NE)_1 + (SW)_1 + (SE)_1 + (NW)_2 + (NE)_2 + (SW)_2 + (SE)_2 + (NE)_3 + (NW)_3 + (SW)_3 + (SE)_3 + (NE)_4 + (NW)_4 \quad (81)$$

Applying symmetry conditions, equation (81) becomes;

$$ML_{Tag15} = K_{WNE}^{1} + K_{WSE}^{1} + K_{WNE}^{2} + K_{WSE}^{2} + K_{WNE}^{3} + K_{WSE}^{3} + K_{WNE}^{4} \quad (82)$$

Applying mirror-image conditions, equation (82) becomes;

$$ML_{Tag15} = K_{WNE}^{1,4} + K_{WSE}^{1} + K_{WNE}^{2,3} + K_{WSE}^{2,3} \quad (83)$$

Rearranging equation (83) in a matrix-like form becomes;

$$ML_{Tag15} = \begin{bmatrix} K_{WNE}^{1,4} & K_{WSE}^{1} \\ K_{WNE}^{2,3} & K_{WSE}^{2,3} \end{bmatrix} \quad (84)$$

From equations (80), and (84), the TL_{Tag15} equation becomes;

$$TL_{Tag15} = 3U_4 + 4U_{1-3} + \begin{bmatrix} K_{WNE}^{1,4} & K_{WSE}^{1} \\ K_{WNE}^{2,3} & K_{WSE}^{2,3} \end{bmatrix} \quad (85)$$

3.16 BS(16)-LDM (1 1 1 1); (All ROI Are THICK)

The boundary shape for this tag is shown in Figure 16:

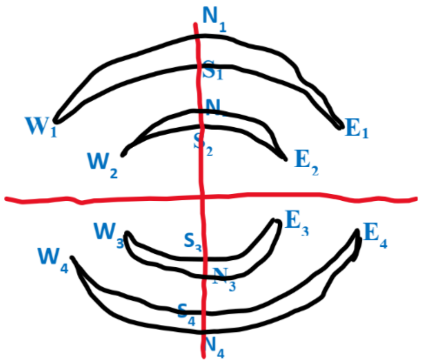

Figure 16. BS(16)-LDM (1 1 1 1) Tag

The TL_{Tag16} for this tag has been derived in C. N. Udekwe & A. A. Ponnle (2019a). It is reproduced here as equation (86);

$$TL_{Tag16} = 4U_4 + \begin{bmatrix} K_{WNE}^{1,4} & K_{WSE}^{1,4} \\ K_{WNE}^{2,3} & K_{WSE}^{2,3} \end{bmatrix} \quad (86)$$

The CPS-LDM equations formulated for each geometric shape with its model tag is show in Table 2.

Table 2. The CPS-LDM Equations for each Model Tag

S/N	Model Tag/ Bit-State	Geometric Shape	CPS-LDM Equation
1	BS(1)-LDM/0000	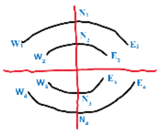	$TL_{Tag1} = \underbrace{3U_M}_{FLs} + \underbrace{\begin{bmatrix} K_{NWE}^{1,4} \\ K_{NWE}^{2,3} \end{bmatrix}}_{MLs}$
2	BS(2)-LDM/0001	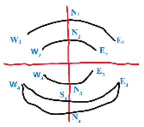	$TL_{Tag2} = 3U_{1-3} + 4U_4 + \begin{bmatrix} K_{WNE}^{1,4} & K_{WSE}^{4} \\ K_{WNE}^{2,3} & - \end{bmatrix}$
3	BS(3)-LDM/0010	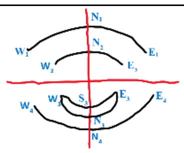	$TL_{Tag3} = 3U_{1-2,4} + 4U_3 + \begin{bmatrix} K_{WNE}^{1,4} & - \\ K_{WNE}^{2,3} & K_{WSE}^{3} \end{bmatrix}$
4	BS(4)-LDM/0011	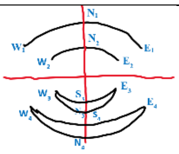	$TL_{Tag4} = 3U_{1-2} + 4U_{3-4} + \begin{bmatrix} K_{WNE}^{1,4} & K_{WSE}^{4} \\ K_{WNE}^{2,3} & K_{WSE}^{3} \end{bmatrix}$
5	BS(5)-LDM/0100	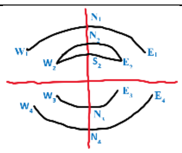	$TL_{Tag5} = 3U_{1,3-4} + 4U_2 + \begin{bmatrix} K_{WNE}^{1,4} & - \\ K_{WNE}^{2,3} & K_{WSE}^{2} \end{bmatrix}$
6	BS(6)-LDM/0101	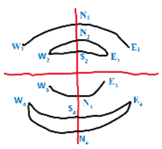	$TL_{Tag6} = 3U_{1,3} + 4U_{2,4} + \begin{bmatrix} K_{WNE}^{1,4} & K_{WSE}^{4} \\ K_{WNE}^{2,3} & K_{WSE}^{2} \end{bmatrix}$

7	BS(7)-LDM/0110	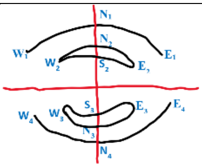	$TL_{Tag7} = 3U_{1,4} + 4U_{2-3} + \begin{bmatrix} K_{WNE}^{1,4} & - \\ K_{WNE}^{2,3} & K_{WSE}^{2,3} \end{bmatrix}$
8	BS(8)-LDM/0111	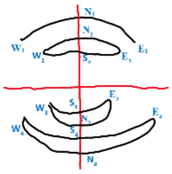	$TL_{Tag8} = 3U_{1} + 4U_{2-4} + \begin{bmatrix} K_{WNE}^{1,4} & K_{WSE}^{4} \\ K_{WNE}^{2,3} & K_{WSE}^{2,3} \end{bmatrix}$
9	BS(9)-LDM/1000	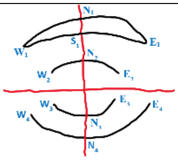	$TL_{Tag9} = 3U_{2-4} + 4U_{1} + \begin{bmatrix} K_{WNE}^{1,4} & K_{WSE}^{1} \\ K_{WNE}^{2,3} & - \end{bmatrix}$
10	BS(10)-LDM/1001	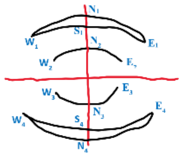	$TL_{Tag10} = 3U_{2-3} + 4U_{1,4} + \begin{bmatrix} K_{WNE}^{1,4} & K_{WSE}^{1,4} \\ K_{WNE}^{2,3} & - \end{bmatrix}$
11	BS(11)-LDM/1010	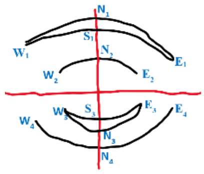	$TL_{Tag10} = 3U_{2-3} + 4U_{1,4} + \begin{bmatrix} K_{WNE}^{1,4} & K_{WSE}^{1,4} \\ K_{WNE}^{2,3} & - \end{bmatrix}$
12	BS(12)-LDM/1011	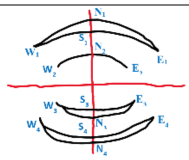	$TL_{Tag12} = 3U_{3} + 4U_{1,3-4} + \begin{bmatrix} K_{WNE}^{1,4} & K_{WSE}^{1,4} \\ K_{WNE}^{2,3} & K_{WSE}^{3} \end{bmatrix}$
13	BS(13)-LDM/1100	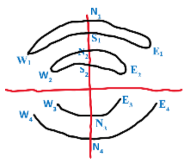	$TL_{Tag13} = 3U_{1-2} + 4U_{3-4} + \begin{bmatrix} K_{WNE}^{1,4} & K_{WSE}^{1} \\ K_{WNE}^{2,3} & K_{WSE}^{2} \end{bmatrix}$
14	BS(14)-LDM/1101	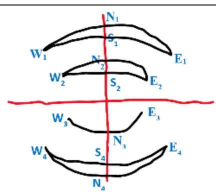	$TL_{Tag14} = 3U_{3} + 4U_{1-2,4} + \begin{bmatrix} K_{WNE}^{1,4} & K_{WSE}^{1,4} \\ K_{WNE}^{2,3} & K_{WSE}^{2} \end{bmatrix}$
15	BS(15)-LDM/1110	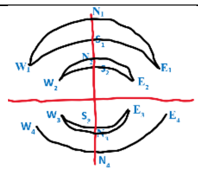	$TL_{Tag15} = 3U_{4} + 4U_{1-3} + \begin{bmatrix} K_{WNE}^{1,4} & K_{WSE}^{1} \\ K_{WNE}^{2,3} & K_{WSE}^{2,3} \end{bmatrix}$
16	BS(16)-LDM/1111	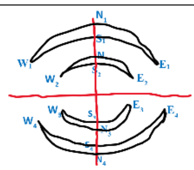	$TL_{Tag16} = 4U_{4} + \begin{bmatrix} K_{WNE}^{1,4} & K_{WSE}^{1,4} \\ K_{WNE}^{2,3} & K_{WSE}^{2,3} \end{bmatrix}$

4. Conclusion

In conclusion, Intima-media thickness (IMT) emerges as a valuable diagnostic marker in the assessment of atherosclerosis within the carotid artery. Ultrasound scans, while the primary imaging modality for IMT measurement, have their limitations, including operator dependency and segmentation challenges. To address these limitations and enhance our understanding of carotid artery health, landmark-based geometric morphometrics (GM) has been introduced. This innovative approach, building upon previous cardinal point symmetry landmark distributed model (CPS-LDM), aims to comprehensively characterize and segment carotid artery IMT, providing valuable insights into variations and alterations.

The proposed Bit-State (BS) Model offers a novel binary representation of carotid artery structural variations, simplifying the complexity of the data. By systematically characterizing shape variations using CPS-LDM equations for each Bit-State, this research paves the way for a deeper understanding of carotid artery health and the impact of atherosclerosis.

In summary, this research contributes to advancing our knowledge of carotid artery health assessment, offering potential avenues for more precise diagnoses and interventions in the realm of cardiovascular health. It highlights the importance of innovative approaches like landmark-based GM in tackling the challenges posed by carotid artery diseases and atherosclerosis.

Examples of how these equations can be used to segment the ROI of a B-Mode ultrasound carotid artery transverse cross-section have been described in the appendixes of our papers (C. N. Udekwe & A. A. Ponnle, 2019a; 2019b; 2021).

References

A. Thapar, I. H. Jenkins, A. Mehta, and A. H. Davies, (2013, March). Diagnosis and management of carotid atherosclerosis. *BMJ*, *346*(7900). doi: 10.1136/BMJ.F1485.

A. Zahalka and A. Fenster, (2001). An automated segmentation method for three-dimensional carotid ultrasound images. *Phys Med Biol*, *46*(4), pp. 1321–1342. doi: 10.1088/0031-9155/46/4/327.

C. M. Moran and A. J. W. Thomson, (2020). Preclinical Ultrasound Imaging — A Review of Techniques and Imaging Applications. *Front Phys*, *8*, p. 516043, doi: 10.3389/FPHY.2020.00124/BIBTEX.

C. N. Udekwe and A. A. Ponnle, (2019a). Cardinal Points Symmetry Landmarks Distribution Model for Segmentation of Region of Interest in Simulated B-Mode Ultrasound Carotid Artery Images. *European Journal of Engineering Research and Science*, *4*(5), pp. 26–33. doi: 10.24018/ejers.2019.4.5.1243.

C. N. Udekwe and A. A. Ponnle, (2019b). Application of Cardinal Points Symmetry Landmarks Distribution Model to B-Mode Ultrasound Images of Transverse Cross-section of Thin-walled Phantom Carotid Arteries. *European Journal of Engineering Research and Science*, *4*(12), pp. 96–101. doi: 10.24018/ejers.2019.4.12.1656.

C. N. Udekwe and A. A. Ponnle, (2021, December). Adaptation of Cardinal Points Symmetry Landmarks Distribution Model to in-vivo B-Mode Ultrasound Images of Transverse Cross-section of Carotid Arteries. *European Journal of Engineering and Technology Research*, *6*(7), pp. 107–113. doi: 10.24018/EJENG.2021.6.7.2633.

Carotid Intima-Media Thickness Test, (n.d.). https://www.radiologyinfo.org/en/info/carotid-intima (accessed Sep. 20, 2023).

Carotid Stenosis | Temple Health, (n.d.). https://www.templehealth.org/services/conditions/carotid-stenosis (accessed Sep. 19, 2023).

D. K. Arnett et al., (2019). 2019 ACC/AHA Guideline on the Primary Prevention of Cardiovascular Disease: A Report of the American College of Cardiology/American Heart Association Task Force on Clinical Practice Guidelines. *Circulation*, *140*(11), NLM (Medline), pp. e596–e646. doi: 10.1161/CIR.0000000000000678.

E. Ukwatta et al., (2011). Three-dimensional ultrasound of carotid atherosclerosis: Semiautomated segmentation using a level set-based method. *Med Phys*, *38*(5), pp. 2479–2493. doi: 10.1118/1.3574887.

G. H. Kim and H. J. Youn, (2017). Is Carotid Artery Ultrasound Still Useful Method for Evaluation of Atherosclerosis? *Korean Circ J*, *47*(1), pp. 1–8. doi: 10.4070/KCJ.2016.0232.

H. Bogunović et al., (2012). Automated landmarking and geometric characterization of the carotid siphon. *Med Image Anal*, *16*(4), pp. 889–903, doi: https://doi.org/10.1016/j.media.2012.01.006.

Ischemic Stroke (Clots): Causes, Symptoms & Treatment, (n.d.). https://my.clevelandclinic.org/health/diseases/24208-ischemic-stroke-clots (accessed Sep. 19, 2023).

J. D. Gill, H. M. Ladak, D. A. Steinman, and A. Fenster, (2000). Accuracy and variability assessment of a semiautomatic technique for segmentation of the carotid arteries from three-dimensional ultrasound images. *Med Phys, 27*(6), pp. 1333–1342. doi: 10.1118/1.599014.

M. L. Bots, G. W. Evans, W. A. Riley, and D. E. Grobbee, (2003). Intima-Media Thickness Measurements in Intervention Studies: Design Options, Progression Rates, and Sample Size Considerations: A Point of View. *Stroke, 34*(12), pp. 2985–2994, doi: 10.1161/01.STR.0000102044.27905.B5.

M. Webster and H. D. Sheets, (2010, October). A Practical Introduction to Landmark-Based Geometric Morphometrics. *The Paleontological Society Papers, 16*, pp. 163–188. doi: 10.1017/S1089332600001868.

Management of symptomatic carotid atherosclerotic disease — UpToDate, (n.d.). https://www.uptodate.com/contents/management-of-symptomatic-carotid-atherosclerotic-disease#! (accessed Sep. 19, 2023).

P. Abolmaesumi, M. R. Sirouspour, and S. E. Salcudean, (2000). Real-time extraction of carotid artery contours from ultrasound images. *Proceedings 13th IEEE Symposium on Computer-Based Medical Systems*. CBMS pp. 181–186. Available: https://api.semanticscholar.org/CorpusID:17797500

R. J. Esper and R. A. Nordaby, (2019). Cardiovascular events, diabetes and guidelines: The virtue of simplicity. *Cardiovascular Diabetology, 18*(1). BioMed Central Ltd., doi: 10.1186/s12933-019-0844-y.